Kinetic inductance coupling for circuit QED with spins

S. Günzler [1,2,*,†] D. Rieger [1,*] M. Spiecker [1,2] T. Koch [1] G. A. Timco [3] R. E. P. Winpenny [3]
I. M. Pop [1,2,4] and W. Wernsdorfer [1,2,‡]

[1]*PHI, Karlsruhe Institute of Technology, 76131 Karlsruhe, Germany*
[2]*IQMT, Karlsruhe Institute of Technology, 76131 Karlsruhe, Germany*
[3]*Photon Science Institute and School of Chemistry, The University of Manchester, Manchester, United Kingdom*
[4]*Physics Institute 1, Stuttgart University, 70569 Stuttgart, Germany*

While transverse coupling (σ_x) is commonly used in qubit-resonator systems, longitudinal coupling via σ_z presents a tantalizing alternative: it does not hybridize the modes, eliminating Purcell decay, and it enables quantum-nondemolition qubit readout independent of the qubit-resonator frequency detuning. Here, we demonstrate longitudinal coupling between a {Cr_7Ni} molecular spin qubit ensemble and the kinetic inductance of a granular aluminum superconducting microwave resonator. The inherent frequency independence of this coupling allows for the utilization of a 7.8-GHz readout resonator to measure the full {Cr_7Ni} magnetization curve spanning 0–600 mT, corresponding to a spin frequency range of $f_{spin} = 0$–15 GHz. For 2-GHz detuning from the readout resonator, we measure a $1/e$ spin relaxation time of $\tau = 0.38$ s, limited by phonon decay to the substrate. Based on these results, we propose a path towards longitudinal coupling of single spins to a superconducting fluxonium qubit.

I. INTRODUCTION

Spin systems are a promising platform for quantum information processing (QIP) due to their intrinsic isolation from the environment, which offers long coherence times [1–4]. However, this isolation also poses a significant challenge for spin manipulation and readout. Superconducting microwave circuits provide a compelling solution within hybrid quantum architectures [5–7], combining their versatile design, quantum-nondemolition (QND) readout, and efficient manipulation with the long coherence times of spin systems. Over the past decade, superconducting microwave resonators have demonstrated strong coupling to spin ensembles in various systems, including vacancy centers in diamond [8], donor atoms in crystalline substrates [9–11], and molecular magnets [12–15]. Despite these achievements, inhomogeneous broadening limits ensemble coherence, and QIP requires precise control over individual spins—a milestone recently achieved through the readout and manipulation of single electron spins [4,16].

These advances rely on transverse coupling between spins and microwave resonators. For the simplest case of a two-level spin system, the resonator microwave field couples to the spin

transverse component: $H_{int}^{\perp} = \hbar g_x \sigma_x(a^{\dagger} + a)$, where g_x is the coupling constant, $a^{\dagger}$ and a are the resonator bosonic operators, and σ_x is the spin Pauli matrix. While mode hybridization due to transverse coupling enables Purcell-effect spin readout [4,10–13,16,17], it is restricted to the cavity frequency and inherently non-QND [18,19]. Longitudinal interaction provides a robust alternative because the spins couple directly to the resonator frequency via σ_z, i.e., $H_{int}^{\parallel} = \hbar g_z \sigma_z a^{\dagger} a$. The longitudinal coupling strength $g_z = \delta\omega/2$ leads to a spin-flip-induced frequency shift, $\delta\omega$. Since $H_{int}^{\parallel}$ commutes with σ_z, it mitigates the limitations of transverse coupling, enabling frequency-independent and QND readout [20–27].

We argue that kinetic inductance presents a promising platform for longitudinal spin coupling, as it can be modulated by magnetic fields or screening currents induced by nearby spins. Superconducting quantum interference devices (SQUIDs) are a potential implementation, where the spin magnetic moment tunes the SQUID critical current [15,28] and the corresponding kinetic inductance. However, SQUID-based designs face challenges, including limited spin-flux coupling in loop geometries—preventing scalability towards single-spin readout [28]—and the intrinsic nonlinearity of Josephson Junctions (JJs), which limits the power dynamic range of microwave devices. Disordered superconductors, such as NbN, NbTiN, InOx, and granular aluminum (grAl), provide a more versatile kinetic inductance for longitudinal coupling [29–38]. These materials offer several key advantages: (i) intrinsic magnetic field susceptibility without requiring a loop geometry, (ii) resilience in Tesla magnetic fields, and (iii) adaptable nonlinearity, which can be significantly lower compared to JJ-based devices [39]. While kinetic inductance magnetometers (KIMs) [40–42] represent an im-
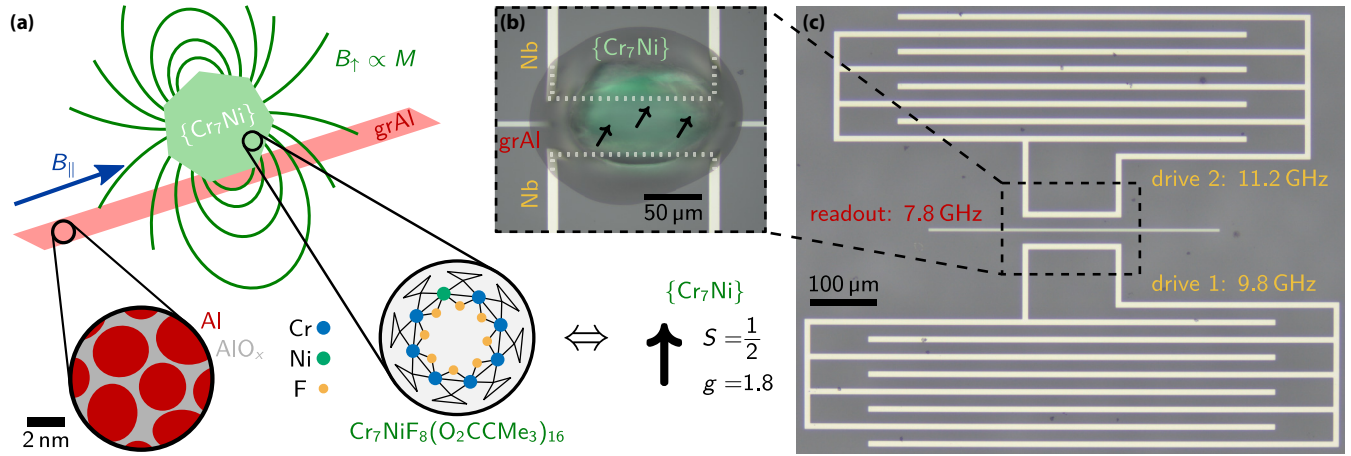
FIG. 1. Implementation of kinetic inductance coupling between a superconducting resonator and molecular spins. (a) Sketch of the resonator-spin system: high-kinetic-inductance granular aluminum (grAl) resonator (red strip) coupled to a {Cr$_7$Ni} microcrystal (green). Left inset: grAl consists of crystalline aluminum grains (red) in an amorphous AlO$_x$ matrix (gray) [38]. Right inset: The single magnetic molecule Cr$_7$NiF$_8$(O$_2$CCMe$_3$)$_{16}$ ≡ {Cr$_7$Ni} has effective spin $S = 1/2$ and $g = 1.8$ [43,44]. The magnetization of the spin ensemble due to the in-plane field $B_\parallel$ (blue arrow) creates the magnetic field $B_\uparrow$ (green lines). This field locally enhances the kinetic inductance of the grAl resonator and provides the mechanism for longitudinal coupling. (b) Optical microscope image of the magnetic crystal (green) placed on top of the grAl readout resonator. The crystal is attached with Apiezon N vacuum grease (transparent gray), which provides thermal conductivity at cryogenic temperatures, low levels of magnetic susceptibility, and low microwave losses (cf. Appendix B). To excite the spins (black arrows) composing the crystal, we use inductively coupled niobium lines, visible above and below the grAl resonator and shown as dashed white outlines in the region underneath the crystal. The 150-μm-long inductor sections of the drive resonators parallel to the central grAl strip generate radio-frequency magnetic fields perpendicular to the spin quantization axis (defined by $B_\parallel$). (c) Zoom-out: The grAl readout resonator (center) is flanked by two low-impedance niobium resonators (top, bottom), necessary to excite the spins. Note that the frequencies $f_{Nb,1}$ and $f_{Nb,2}$ of the niobium drive resonators are several GHz detuned from the readout f_r.

portant step forward, the longitudinal coupling of spins to a microwave device has yet to be demonstrated. In this work, we demonstrate longitudinal coupling between a {Cr$_7$Ni} molecular spin qubit ensemble and the kinetic inductance of a grAl microwave resonator. The spin-ensemble polarization is encoded in the resonator frequency, independent of the spin-resonator detuning, enabling us to perform a full microwave readout of the magnetization curve. Moreover, we demonstrate time-resolved measurement of spin-ensemble excitation and decay at GHz detuning from the readout. Finally, we propose a scheme to achieve single-spin longitudinal coupling to a superconducting fluxonium qubit.

II. RESULTS AND DISCUSSION

Figure 1 illustrates the conceptual implementation of longitudinal coupling between a microwave resonator and a spin ensemble. The magnetic molecules are grown in a single crystal of chemically identical units, composed of eight chromium atoms with one substituted by nickel, which resemble cyclic wheels [cf. bottom right inset in Fig. 1(a)]. Each molecule has an effective spin of $S = 1/2$ and a gyromagnetic factor of $g \approx 1.8$ [43–45], chosen with $g \neq 2$ in order to distinguish from spurious coupling to electronic spins in the environment of superconducting devices [29,30,35,46]. The molecular crystal is placed at the center of a grAl stripline resonator with a resonance frequency of $f_r = 7.8$ GHz and an internal quality factor of $Q_i > 10^5$ (cf. Appendix B). The grAl film has a kinetic inductance fraction of $\alpha \approx 1$ [36] (sheet inductance $L_\square = 0.9$ nH$\square^{-1}$) which arises from its microstructure, effec-

tively forming a three-dimensional network of JJs [38,39,47]. To drive the spin ensemble using microwave transverse fields, on the same chip [cf. Figs. 1(b) and 1(c)], we pattern two low-impedance resonators ($f_{Nb,1} = 9.8$ GHz, $f_{Nb,2} = 11.2$ GHz) made of niobium, which can sustain relatively high current densities.

The longitudinal spin-resonator interaction arises from the coupling of the spin magnetic moments $\mu = -g\mu_B\sigma_z/2$ to the resonator's kinetic inductance L_{kin}, where μ_B denotes the Bohr magneton. The spin-ensemble magnetization M increases L_{kin} and shifts the resonator frequency f_r by δf_M:

$$\delta f_M/f_{r,0} \propto -M^2 . \tag{1}$$

This frequency shift results from persistent currents I_p induced by the perpendicular component $B_{\uparrow,\perp}$ of the sample-generated magnetic field $B_\uparrow \propto M$. These currents locally increase the kinetic inductance $L_{kin}(I_p) \approx L_{kin,0}[1 + (I_p/I^*)^2]$, where I^* characterizes the grAl nonlinearity and is typically on the order of the critical current [40,48]. Given that the grAl effective penetration depth exceeds the resonator width by orders of magnitude [49,50], we consider $I_p \propto B_{\uparrow,\perp}$. Note that the contribution of the superconducting gap suppression to δf_M is neglected, as the persistent current suppression dominates by 3 orders of magnitude for our resonator geometry [35].

Using the grAl resonator, in Fig. 2, we demonstrate the measurement of the {Cr$_7$Ni} crystal magnetization curve in parallel magnetic field $B_\parallel$. The observed frequency shift $\delta f_r(B_\parallel, M)$ [cf. Fig. 2(a)] consists of two contributions: the shift δf_M from the crystal magnetization M [cf. Eq. (1)] and
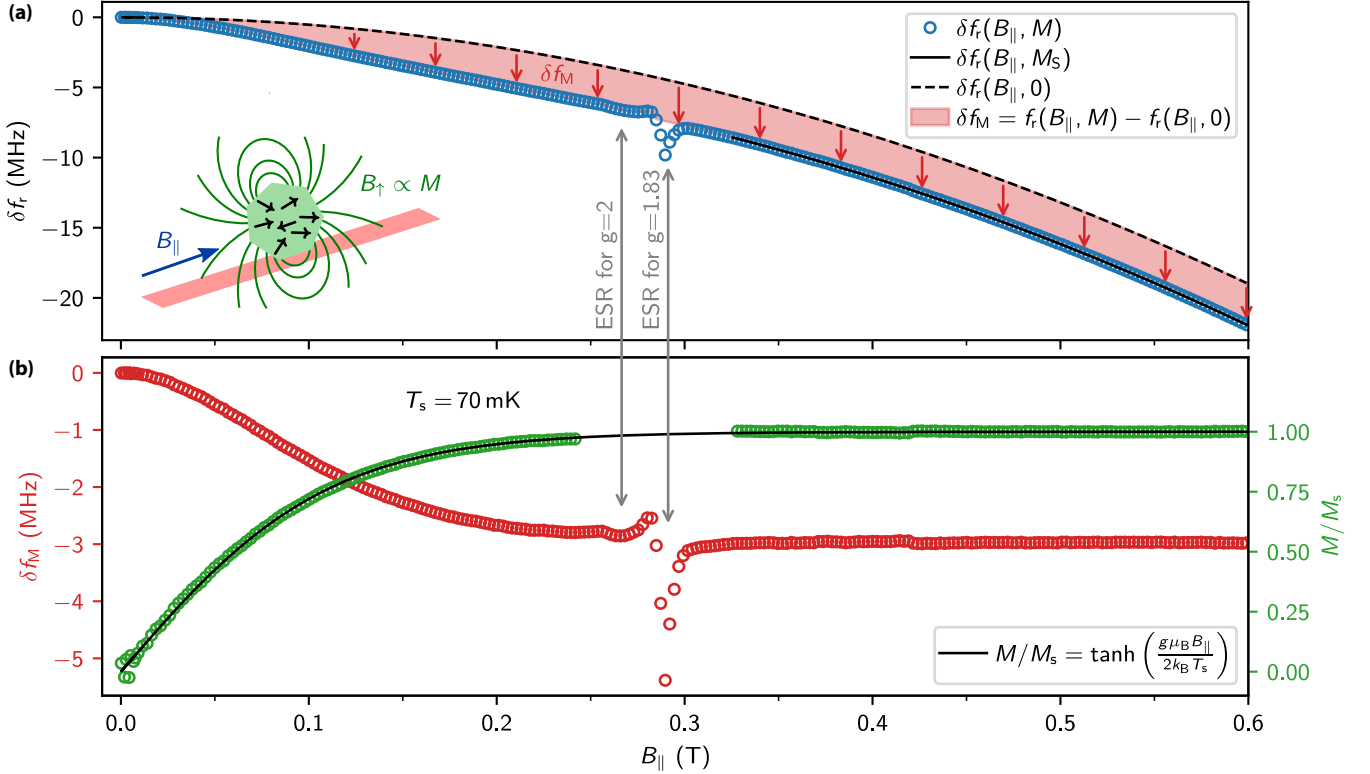
FIG. 2. Detuning-independent readout of the spin-ensemble magnetization. (a) Resonance frequency shift of the grAl readout resonator coupled to the molecular spin ensemble $\delta f_r(B_\parallel, M)$ (blue markers) in the magnetic field. The parabolic frequency shift of the bare resonator $\delta f_r(B_\parallel, M = 0)$ (black dashed line) is given by the suppression of the grAl superconducting gap $\delta(B_\parallel)$ in the magnetic field [35]. The resonator experiences an additional frequency shift δf_M due to the magnetization of the spin ensemble (red shift), yielding the measured total frequency shift $\delta f_r(B_\parallel, M)$. To disentangle these two contributions, we fit a parabolic frequency shift, $\delta f_r(B_\parallel, M_S)$, to the tail of the data for $B_\parallel > 0.32$ T (black solid) where the magnetization of the crystal is saturated ($M = M_S$). We can then remove the vertical offset to get $\delta f_r(B_\parallel, 0)$ (dashed black) and δf_M (red arrows). At $B_\parallel = 0.29$ T, as expected for $g = 1.83$, we measure an avoided level crossing due to the transverse coupling of the spin ensemble to the geometric inductance of the resonator. At $B_\parallel = 0.26$ T, we observe an additional feature corresponding to transverse coupling of $g = 2$ spurious electron spin resonance (ESR) [29,30,35,46]. (b) Extracted frequency shift δf_M (red markers) due to the magnetic field of the crystal and corresponding magnetization $M \propto \sqrt{\delta f_M}$ (green markers). Above $B_\parallel = 0.32$ T, the crystal magnetization saturates, and δf_M remains constant. In the range $B_\parallel = 0.244$–0.302 T, anticrossings (see double arrow markers) arising from residual transverse coupling to $g = 2$ and $g = 1.83$ spins prevent a reliable extraction of the magnetization. Note that the magnetization curve shown here is measured on a sample without Nb drive resonators (cf. Fig. 1) in order to avoid field distortions (cf. Appendix C).

an additional parabolic frequency decrease due to the grAl gap suppression in $B_\parallel$ [35]. To disentangle these effects, we fit the parabolic tail of the frequency shift $\delta f_r(B_\parallel, M_S)$ in the field range where the ensemble magnetization is saturated ($M = M_S$), specifically for $B_\parallel > 0.32$ T in Fig. 2(a). Subtracting the fitted parabolic response $\delta f_r(B_\parallel, 0)$ [dashed line in Fig. 2(a)] from the measured data $\delta f_r(B_\parallel, M)$ isolates the contribution δf_M from the crystal's magnetization, shown in Fig. 2(b). In addition, due to the resonator's geometric inductance, near $B_\parallel = 0.29$ T we observe small transverse couplings to the $g = 1.83$ spins and to spurious $g = 2$ spin impurities.

The magnetization curve in Fig. 2(b), extracted from δf_M using Eq. (1), increases from $M = 0$ to saturation $M = M_S$ in fields above 300 mT. It follows the paramagnetic response $M = M_S \tanh(\frac{g\mu_B B_\parallel}{2k_B T_S})$ for a spin-1/2 ensemble, from which we fit a spin temperature of $T_S = 70$ mK (k_B is the Boltzmann constant). Notably, T_S is above the cryostat temperature of $T \approx 30$ mK, indicating limited thermalization of the molec-

ular spin crystal via the vacuum grease (cf. Fig. 1). In a subsequent run with a smaller crystal, we extract a spin temperature of $T_S = 30$ mK (cf. Appendix C), illustrating the challenge of thermalizing the ensemble—an issue commonly referred to as the phonon bottleneck [51]. To conclude the spin-ensemble characterization, we leverage the detuning-independent nature of the kinetic inductance readout, which remains effective during spin manipulation via the transversely coupled Nb resonators. As shown in Fig. 3(a), we perform two-tone spectroscopy of the spins around 9.85 GHz, 2 GHz detuned from the readout resonator, and we measure $g = 1.83 \pm 0.01$ (black dashed line), comparable to values reported in the literature [43,45]. The excitation pattern reflects the expected convolution of the frequency-dependent drive amplitude, shaped by the Nb resonator's Lorentzian response, combined with the spin ensemble's inhomogeneous linewidth. This measurement confirms that longitudinal readout remains unaffected by transverse driving mediated through auxiliary circuit elements.
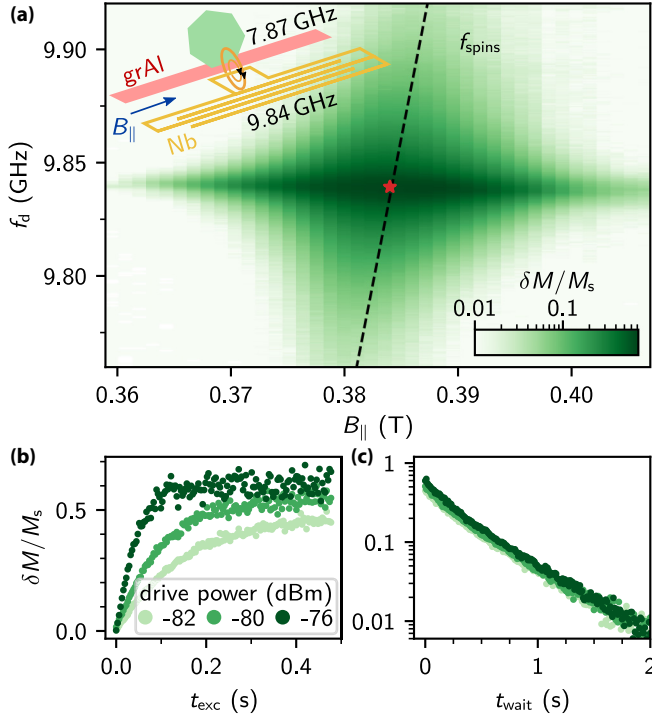
FIG. 3. Excitation and decay of the spin ensemble 2 GHz detuned from the readout. (a) Continuous wave two-tone spectroscopy of the spin ensemble. To excite the spins, we sweep a drive tone f_d in the vicinity of the niobium resonator frequency $f_{Nb1} = 9.84$ GHz while monitoring the readout resonator at $f_r = 7.87$ GHz. The relative change of the ensemble magnetization $\delta M/M_S$ (green colorbar) is calibrated to the measured shift in f_r utilizing a magnetization curve [cf. Fig. 2(b)]. The excitation of the spin ensemble is only effective within the bandwidth $\kappa/2\pi = 2$ MHz of the Nb drive resonator. The dashed line indicates the center frequency of the spin distribution given by $hf = g\mu_B B_\parallel$, with $g = 1.83 \pm 0.01$. (b), (c) Time-domain characterization of the spin ensemble at $B_\parallel = 0.384$ T [red marker in panel (a)]: excitation to saturation (b) and decay from saturation (c) for different drive powers, with a $1/e$ time $\tau = 0.38$ s.

On resonance with the Nb drive [red marker in Fig. 3(a)], we measure time-resolved excitation and decay of the ensemble magnetization [cf. Figs. 3(b) and 3(c)]. We observe a nonexponential decay with $1/e$ reached after $\tau = 0.38$ s. This lifetime, significantly longer than reported for the same {Cr$_7$Ni} molecules in solution [44], is likely limited by the decay of the crystal phonons into the substrate. In fact, the much lower heat capacity of the phonon bath compared to that of the spins leads to a phonon bottleneck [51,52]. Reducing the number of spins could mitigate this limitation, ultimately aiming to reach the single-spin regime. Note that we exclude drive-induced heating as the origin of the spin excitation, since the ensemble magnetization remains unchanged when the spins are detuned from the drive [e.g., at $B_\parallel = 0.36$ T in Fig. 3(a)].

III. OUTLOOK

While we estimate that approximately 10^{11} spins within the molecular crystal contribute to the readout signal in Figs. 2
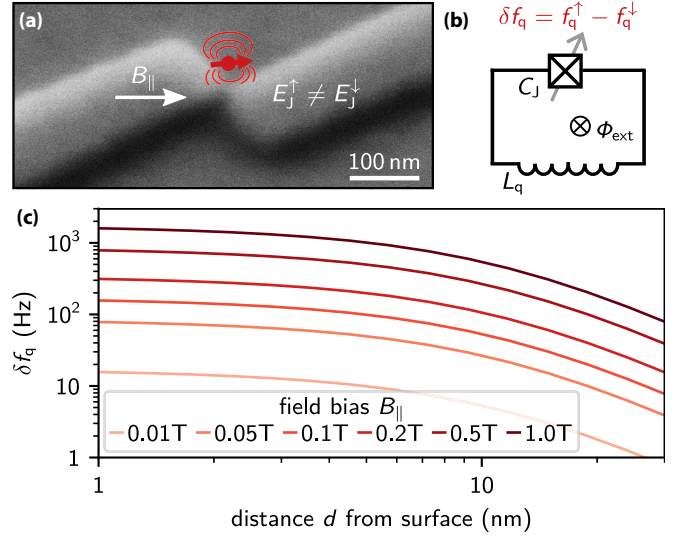

FIG. 4. Towards longitudinal coupling between superconducting circuits and single spins. (a) Implementation of a spin-modulated Josephson junction: scanning electron microscope image of a grAl nanojunction with a single spin sketched on top. The nanojunction consists of an $\approx (20$ nm$)^3$ grAl volume [47], which remains coherent in Tesla-scale magnetic fields [46]. When biased in the magnetic field $B_\parallel$, the two spin orientations generate different local magnetic fields, leading to distinct Josephson energies $E_J^\uparrow$ and $E_J^\downarrow$. (b) We use the spin-state-dependent nanojunction to build a fluxonium quantum circuit with the junction capacitance C_J, the superinductor L_q, and the external flux Φ_{ext}. The spin polarization tunes the Josephson energy E_J and, consequently, the fluxonium transition frequency f_q. (c) Simulation of the qubit frequency shift δf_q for a spin-flip versus distance d from the nanojunction surface for several $B_\parallel$ bias values. Note that for the calculation we used a spin with magnetic moment $\mu = 10\,\mu_B$ (see Ref. [15]) on top of a regular gralmonium qubit [47].

and 3, sensitivity can be further enhanced by adopting loop-based geometries akin to KIMs [40–42] and narrowing the resonator width to increase kinetic inductance nonlinearity at a constant persistent loop current. Figure 4 extends the idea of tailoring the readout circuit by proposing a kinetic-inductance-based coupling scheme designed for single-spin detection, utilizing established grAl circuit elements. To obtain longitudinal coupling to the highly localized dipole field of a single spin, we need to concentrate the kinetic inductance within a nanoscopic volume. This volume reduction inherently increases device nonlinearity [39], which for the 20-nm cross section in Fig. 4(a) effectively results in a Josephson junction, referred to as a grAl nanojunction [47]. The spin-dependent local magnetic field threading the nanojunction locally induces a quadratic suppression of the grAl superconducting gap Δ, resulting in a spin-state-dependent Josephson energy E_J: $E_J^\uparrow \neq E_J^\downarrow$.

We propose embedding the grAl nanojunction into a fluxonium quantum circuit operated at the half-flux sweet spot, where the qubit frequency is exponentially sensitive to variations in E_J [47]. The resulting circuit shown in Fig. 4(b) can be described by the standard fluxonium Hamiltonian

$$H_{flux} = 4E_C n^2 + \frac{1}{2}E_L\left(\varphi - 2\pi\frac{\Phi_{ext}}{\Phi_0}\right)^2 - E_J\cos\varphi, \quad (2)$$
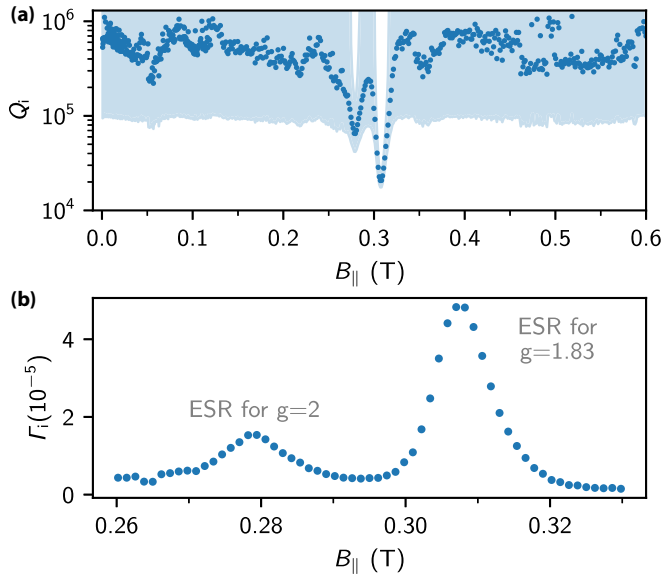
FIG. 5. Resilience of grAl resonators in a parallel field. Internal quality factor Q_i (blue markers) corresponding Fano uncertainty range [56] (blue shaded area) of the grAl resonator in the magnetic field $B_\parallel$. The resonator is measured at an average photon number of $\bar{n} \approx 10$ with a coupling quality factor of $Q_c = 25 \times 10^3$. The dips in Q_i, shown as peaks in the decay rate $\Gamma_i = 1/Q_i$ in panel (b), correspond to ESR of spurious electronic spins with $g = 2$ (left) and the molecular spin ensemble with $g = 1.83$ (right). The associated resonance frequency shifts are presented in Fig. 7.
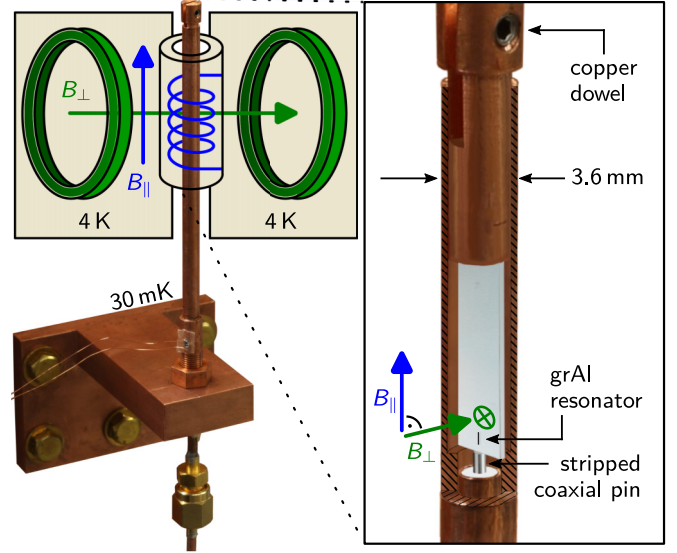

FIG. 6. Sample holder and magnetic field configuration. Photograph of the cylindrical waveguide sample holder with a schematic of the two-dimensional vector magnet, showing the directions of applied magnetic fields parallel and perpendicular to the chip plane. Inset: Cross-sectional view of the sample holder. The grAl resonator, fabricated on a sapphire chip, is coupled via the evanescent field of a stripped microwave coaxial pin. A Helmholtz coil pair, oriented perpendicular to the chip plane, compensates for misalignment between the solenoid coil's field and the chip plane. Adapted from Ref. [46], licensed under CC BY 4.0.

where $E_L = (\Phi_0/2\pi)^2/L_q$ and $E_C = e^2/2C$ denote the fluxonium inductive and charging energies, respectively. Besides the trivial modulation from the bias field $B_\parallel$, $E_J = E_J(B_\parallel, \sigma_z)$ also depends on the spin qubit state σ_z, thereby implementing a longitudinal coupling where σ_z commutes with H_{flux}. A practical realization of such a circuit should be resilient to the high magnetic fields required for spin qubit operation, as recently demonstrated in a gradiometric geometry in Ref. [46].

To estimate the fluxonium qubit frequency shift δf_q due to a spin flip in a realistic scenario, we model the spin as a pointlike magnetic dipole with a magnetic moment of $\mu = 10 \, \mu_B$ oriented (anti-)parallel to the bias field $B_\parallel$. Spins with such large magnetic moments can be engineered in single-molecule magnets with strong anisotropy, forming an effective two-level-system [15]. For a spin centered at a distance d above the nanojunction, we numerically calculate the local grAl gap suppression $\Delta(\vec{B}_\uparrow(\vec{r}) + \vec{B}_\parallel)/\Delta(0) = \sqrt{1 - (|\vec{B}_\uparrow(\vec{r}) + \vec{B}_\parallel|/B_c)^2}$ [53] at position $\vec{r}$ within its $(20 \text{ nm})^3$ volume. By numerically solving Eq. (2) for the corresponding $E_J \propto \iiint d\vec{r} \, \Delta(\vec{r})$, we find the qubit frequency shift δf_q, shown in Fig. 4(c). Positioning the spin as close as possible to the nanojunction and operating in the $B_\parallel \sim 10^2$ mT range enables spin-state-dependent frequency shifts δf_q on the order of kHz. Given that superconducting qubit frequencies can be resolved with kHz-accuracy [54,55], we are optimistic that longitudinal coupling via kinetic inductance will enable single-shot QND readout of individual spins.

IV. CONCLUSION

In conclusion, we have demonstrated longitudinal coupling between a {Cr$_7$Ni} molecular spin ensemble and a grAl superconducting microwave resonator via kinetic inductance, enabling frequency-independent and nondemolishing spin readout. The independence of the readout contrast on detuning between the spins and the resonator allowed us to measure the full magnetization curve over a field range of hundreds of mT and observe time-resolved spin dynamics at GHz detuning. To overcome ensemble limitations like inhomogeneous broadening and the phonon relaxation bottleneck, we propose extending this longitudinal coupling scheme to a single spin positioned in the close vicinity of a grAl nanojunction in a fluxonium qubit. For state-of-the-art grAl devices, our simulations predict a spin-dependent qubit frequency shift up to kHz, opening the path for QND interaction at the single-spin level. Order of magnitude stronger interaction could be possible by miniaturizing the nanojunction by a factor of 2 and embedding the magnetic molecule in its center.
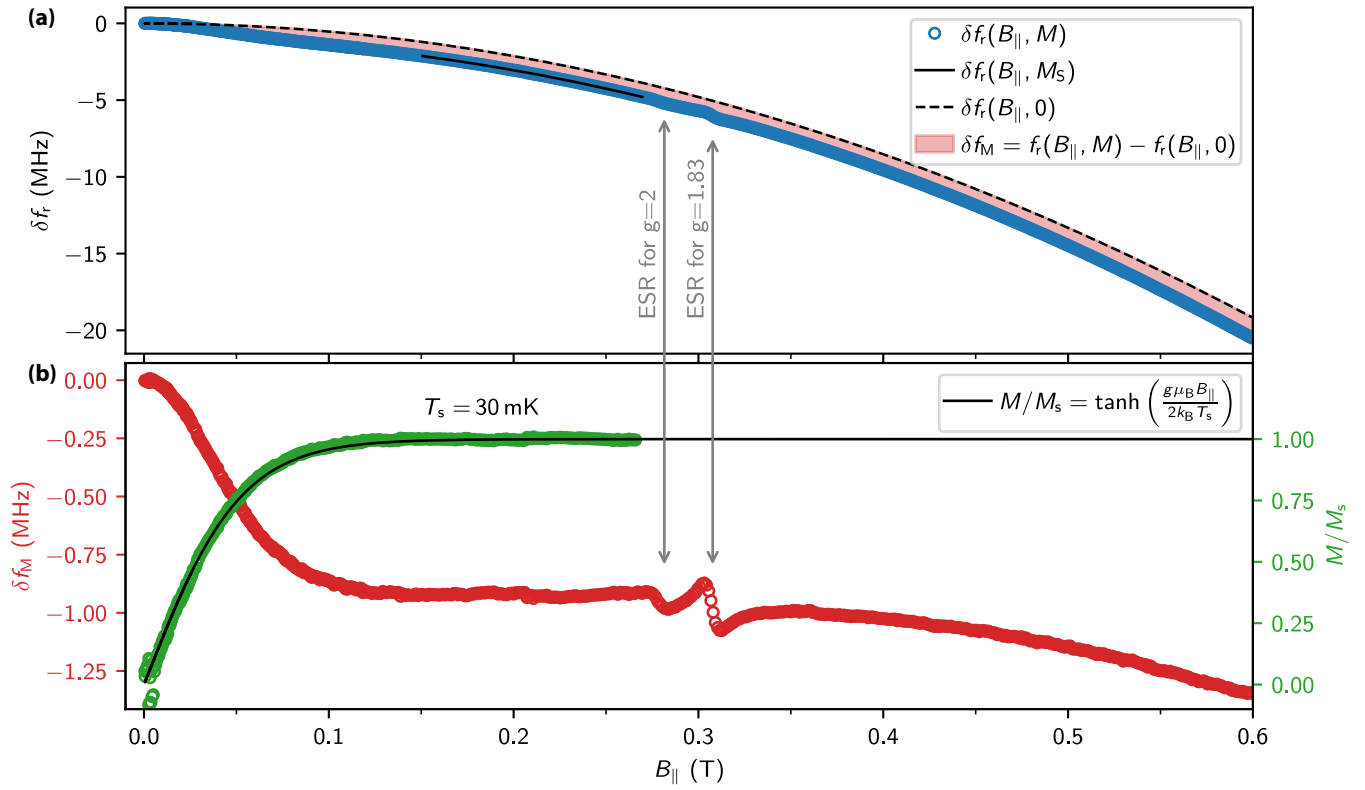
FIG. 7. Readout of the spin-ensemble magnetization in the presence of on-chip Nb drive resonators. (a) Resonance frequency shift $\delta f_r(B_\parallel, M)$ (blue markers) of the grAl readout resonator coupled to the molecular spin ensemble, measured in the presence of Nb drive resonators (which remain undriven during this measurement). To extract the magnetization $M \propto \sqrt{\delta f_M}$ (green markers) in panel (b), we fit the parabolic frequency shift $\delta f_r(B_\parallel, M_S)$ for saturated spin crystal magnetization ($M = M_S$) in the range $B_\parallel = 150$–270 mT and follow the main text procedure (cf. Fig. 2). For fields above $B_\parallel = 0.27$ T, as shown by the frequency shift δf_M (red markers) in panel (b), anticrossings arising from residual transverse coupling to $g = 2$ and $g = 1.83$ spins (gray arrows) as well as screening fields from the superconducting Nb structures distort the extracted frequency shift δf_M.

Laboratory (NSL). We acknowledge QKIT for providing a convenient measurement software framework.

DATA AVAILABILITY

The data that support the findings of this article are not publicly available upon publication because it is not technically feasible and/or the cost of preparing, depositing, and hosting the data would be prohibitive within the terms of this research project. The data are available from the authors upon reasonable request.

APPENDIX A: FABRICATION DETAILS

The resonators discussed in this paper are fabricated on a double-side-polished c-plane sapphire substrate. They are patterned using lift-off optical lithography with AZ5214E photoresist, followed by development in AZ developer. Before metal deposition, an Ar/O_2 plasma cleaning step is performed using a Kaufman ion source. Additionally, a titanium gettering step reduces the chamber pressure to $p \sim 10^{-7}$ mbar before evaporation in a Plassys MEB 550S shadow evaporation system. The 20-nm granular aluminum (grAl) film is deposited at 1 nm/s, yielding a sheet resistance of $1.1 \, k\Omega/\square$. In a second lithography step, 50-nm-thick niobium drive resonators are

patterned and deposited with an evaporation rate of 1 nm/s, using the same optical procedure.

APPENDIX B: GRAL RESONATOR IN MAGNETIC FIELD

In Fig. 5, we confirm the resilience of the grAl readout resonator in the parallel magnetic field $B_\parallel$. The internal quality factor remains above $Q_i \gtrsim 10^5$, even when accounting for systematic Fano uncertainty in the loss measurement [56], except for two distinct dips. These increased losses occur where the resonator frequency matches the ESR of the $g = 1.83$ molecular spin ensemble and of spurious $g = 2$ spins, commonly observed in the environment of superconducting devices [29,30,35,46]. The latter can serve as an *in situ* calibration of the on-chip magnetic field strength.

Notably, the quality factors of the grAl resonator are not affected by the Apiezon N vacuum grease on top, used to thermalize and attach the crystal (cf. Fig. 1). Within the uncertainty, the values reported in Fig. 5 are equivalent to values reported in the literature [35,36,56] and could be further improved by an order of magnitude for optimized geometry, substrate, and cleaning procedures, as shown in Ref. [57].

Beyond field strength, we also calibrate the field direction to ensure that all measurements in this paper are performed

with $B_{\parallel}$ strictly aligned with the substrate plane. This prevents hysteretic, nonmonotonic resonance frequency shifts and additional perpendicular field ($B_{\perp}$) effects that would complicate the extraction of δf_M. To compensate for minor chip misalignments within our cylindrical sample holder (cf. Fig. 6; identical to Refs. [35,46,56]) we introduce an out-of-plane compensation field $B_{\perp,\mathrm{comp}}$ for each applied $B_{\parallel}$. We determine $B_{\perp,\mathrm{comp}}$ by sweeping the perpendicular field component $B_{\perp}$ and maximizing the resonator frequency.

APPENDIX C: ADDITIONAL MAGNETIZATION CURVE

In Fig. 7, we confirm that the presence of the Nb drive resonators, which introduces magnetic field distortions, still allows reliable extraction of the spin-ensemble magnetization. As shown in Fig. 1, these Nb resonators are patterned directly adjacent to the grAl readout resonator. The extracted shift δf_M and corresponding magnetization M, shown in Fig. 7(b), exhibit saturation behavior similar to the sample without Nb resonators (cf. Fig. 2). The frequency shift at saturation $\delta f_M(M_S)$ is smaller compared to Fig. 2 due to the use of a smaller molecular crystal. From a fit to the paramagnetic response $M = M_S \tanh(\frac{g\mu_B B_{\parallel}}{2k_B T_S})$ for a spin-1/2 ensemble, we extract a spin temperature of $T_S = 30$ mK. We attribute the lower spin temperature compared to Fig. 2 to the higher surface-to-volume ratio of the smaller crystal, which enhances phonon decay into the substrate. For bias fields above $B_{\parallel} > 300$ mT, the magnetization remains constant, but an additional shift in δf_M arises due to out-of-plane magnetic fields generated by screening currents in the niobium structures of the drive resonators.

APPENDIX D: TOWARDS LONGITUDINAL COUPLING TO A SINGLE SPIN

A single spin positioned directly atop a granular aluminum nanojunction modifies the local superconducting gap
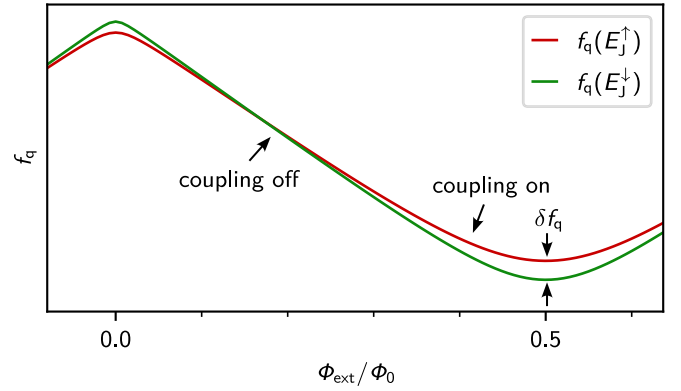

FIG. 8. Simulated fluxonium qubit spectrum for the spin-dependent Josephson energy E_J. Transition frequency f_q of a fluxonium qubit as a function of the external flux Φ_{ext}, for two values of the Josephson energy E_J. The two spin states of a magnetic moment located atop the grAl nanojunction lead to $E_J^{\uparrow} \neq E_J^{\downarrow}$, corresponding to the flux-dependent fluxonium qubit frequency shift δf_q. The coupling strength is exaggerated for visual clarity.

via its magnetic field, resulting in the spin-state-dependent Josephson energy $E_J^{\uparrow} \neq E_J^{\downarrow}$. Embedding such a nanojunction into a fluxonium circuit realizes a longitudinal spin-fluxonium interaction, where the spin state shifts the fluxonium transition frequency f_q by an amount δf_q. This frequency shift depends on the external flux bias Φ_{ext}, reaching a maximum at the half-flux sweet spot ($\Phi_{\mathrm{ext}} = 0.5\,\Phi_0$), where the fluxonium is most sensitive to variations in E_J.

Figure 8 illustrates the principle of longitudinal spin–fluxonium coupling by showing the simulated qubit spectrum for two distinct values of E_J, corresponding to the two spin orientations. The two spectra cross at a specific flux bias where $f_q(E_J^{\uparrow}) = f_q(E_J^{\downarrow})$, defining the operating point at which the longitudinal coupling vanishes. This flux tunability provides a valuable handle for modulating the interaction strength *in situ*.

[1] G. Burkard, T. D. Ladd, A. Pan, J. M. Nichol, and J. R. Petta, Semiconductor spin qubits, Rev. Mod. Phys. **95**, 025003 (2023).

[2] M. Zhong, M. P. Hedges, R. L. Ahlefeldt, J. G. Bartholomew, S. E. Beavan, S. M. Wittig, J. J. Longdell, and M. J. Sellars, Optically addressable nuclear spins in a solid with a six-hour coherence time, Nature (London) **517**, 177 (2015).

[3] D. Serrano, S. K. Kuppusamy, B. Heinrich, O. Fuhr, D. Hunger, M. Ruben, and P. Goldner, Ultra-narrow optical linewidths in rare-earth molecular crystals, Nature (London) **603**, 241 (2022).

[4] J. O'Sullivan, J. Travesedo, L. Pallegoix, Z. W. Huang, A. May, B. Yavkin, P. Hogan, S. Lin, R. Liu, T. Chaneliere, S. Bertaina, P. Goldner, D. Esteve, D. Vion, P. Abgrall, P. Bertet, and E. Flurin, Individual solid-state nuclear spin qubits with coherence exceeding seconds, arXiv:2410.10432.

[5] G. Kurizki, P. Bertet, Y. Kubo, K. Mølmer, D. Petrosyan, P. Rabl, and J. Schmiedmayer, Quantum technologies with hybrid systems, Proc. Natl. Acad. Sci. USA **112**, 3866 (2015).

[6] Z.-L. Xiang, S. Ashhab, J. Q. You, and F. Nori, Hybrid quantum circuits: Superconducting circuits interacting with other quantum systems, Rev. Mod. Phys. **85**, 623 (2013).

[7] A. A. Clerk, K. W. Lehnert, P. Bertet, J. R. Petta, and Y. Nakamura, Hybrid quantum systems with circuit quantum electrodynamics, Nat. Phys. **16**, 257 (2020).

[8] Y. Kubo, F. R. Ong, P. Bertet, D. Vion, V. Jacques, D. Zheng, A. Dréau, J.-F. Roch, A. Auffeves, F. Jelezko, J. Wrachtrup, M. F. Barthe, P. Bergonzo, and D. Esteve, Strong coupling of a spin ensemble to a superconducting resonator, Phys. Rev. Lett. **105**, 140502 (2010).

[9] D. I. Schuster, A. P. Sears, E. Ginossar, L. DiCarlo, L. Frunzio, J. J. L. Morton, H. Wu, G. A. D. Briggs, B. B. Buckley, D. D. Awschalom, and R. J. Schoelkopf, High-cooperativity coupling of electron-spin ensembles to superconducting cavities, Phys. Rev. Lett. **105**, 140501 (2010).

[10] A. Bienfait, J. J. Pla, Y. Kubo, M. Stern, X. Zhou, C. C. Lo, C. D. Weis, T. Schenkel, M. L. W. Thewalt, D. Vion, D. Esteve,

B. Julsgaard, K. Mølmer, J. J. L. Morton, and P. Bertet, Reaching the quantum limit of sensitivity in electron spin resonance, Nat. Nanotechnol. **11**, 253 (2016).

[11] C. Eichler, A. J. Sigillito, S. A. Lyon, and J. R. Petta, Electron spin resonance at the level of 10^4 spins using low impedance superconducting resonators, Phys. Rev. Lett. **118**, 037701 (2017).

[12] C. Bonizzoni, A. Ghirri, M. Atzori, L. Sorace, R. Sessoli, and M. Affronte, Coherent coupling between vanadyl phthalocyanine spin ensemble and microwave photons: Towards integration of molecular spin qubits into quantum circuits, Sci. Rep. **7**, 13096 (2017).

[13] M. Mergenthaler, J. Liu, J. J. Le Roy, N. Ares, A. L. Thompson, L. Bogani, F. Luis, S. J. Blundell, T. Lancaster, A. Ardavan, G. A. D. Briggs, P. J. Leek, and E. A. Laird, Strong coupling of microwave photons to antiferromagnetic fluctuations in an organic magnet, Phys. Rev. Lett. **119**, 147701 (2017).

[14] I. Gimeno, W. Kersten, M. C. Pallarés, P. Hermosilla, M. J. Martínez-Pérez, M. D. Jenkins, A. Angerer, C. Sánchez-Azqueta, D. Zueco, J. Majer, A. Lostao, and F. Luis, Enhanced molecular spin-photon coupling at superconducting nanoconstrictions, ACS Nano **14**, 8707 (2020).

[15] E. Moreno-Pineda and W. Wernsdorfer, Measuring molecular magnets for quantum technologies, Nat. Rev. Phys. **3**, 645 (2021).

[16] Z. Wang, L. Balembois, M. Rančić, E. Billaud, M. Le Dantec, A. Ferrier, P. Goldner, S. Bertaina, T. Chanelière, D. Esteve, D. Vion, P. Bertet, and E. Flurin, Single-electron spin resonance detection by microwave photon counting, Nature (London) **619**, 276 (2023).

[17] A. Bienfait, J. J. Pla, Y. Kubo, X. Zhou, M. Stern, C. C. Lo, C. D. Weis, T. Schenkel, D. Vion, D. Esteve, J. J. L. Morton, and P. Bertet, Controlling spin relaxation with a cavity, Nature (London) **531**, 74 (2016).

[18] A. Blais, A. L. Grimsmo, S. M. Girvin, and A. Wallraff, Circuit quantum electrodynamics, Rev. Mod. Phys. **93**, 025005 (2021).

[19] M. F. Dumas, B. Groleau-Paré, A. McDonald, M. H. Muñoz-Arias, C. Lledó, B. D'Anjou, and A. Blais, Measurement-induced transmon ionization, Phys. Rev. X **14**, 041023 (2024).

[20] N. Didier, J. Bourassa, and A. Blais, Fast quantum nondemolition readout by parametric modulation of longitudinal qubit-oscillator interaction, Phys. Rev. Lett. **115**, 203601 (2015).

[21] S. Richer and D. DiVincenzo, Circuit design implementing longitudinal coupling: A scalable scheme for superconducting qubits, Phys. Rev. B **93**, 134501 (2016).

[22] R. Dassonneville, T. Ramos, V. Milchakov, L. Planat, É. Dumur, F. Foroughi, J. Puertas, S. Leger, K. Bharadwaj, J. Delaforce, C. Naud, W. Hasch-Guichard, J. J. García-Ripoll, N. Roch, and O. Buisson, Fast high-fidelity quantum nondemolition qubit readout via a nonperturbative Cross-Kerr coupling, Phys. Rev. X **10**, 011045 (2020).

[23] A. A. Chapple, A. McDonald, M. H. Muñoz-Arias, and A. Blais, Robustness of longitudinal transmon readout to ionization, arXiv:2412.07734.

[24] R. Ruskov and C. Tahan, Quantum-limited measurement of spin qubits via curvature couplings to a cavity, Phys. Rev. B **99**, 245306 (2019).

[25] C. G. L. Bøttcher, S. P. Harvey, S. Fallahi, G. C. Gardner, M. J. Manfra, U. Vool, S. D. Bartlett, and A. Yacoby, Parametric longitudinal coupling between a high-impedance superconducting resonator and a semiconductor quantum dot singlet-triplet spin qubit, Nat. Commun. **13**, 4773 (2022).

[26] S. Bosco, P. Scarlino, J. Klinovaja, and D. Loss, Fully tunable longitudinal spin-photon interactions in Si and Ge quantum dots, Phys. Rev. Lett. **129**, 066801 (2022).

[27] B. Harpt, J. Corrigan, N. Holman, P. Marciniec, D. Rosenberg, D. Yost, R. Das, R. Ruskov, C. Tahan, W. D. Oliver, R. McDermott, M. Friesen, and M. A. Eriksson, Ultra-dispersive resonator readout of a quantum-dot qubit using longitudinal coupling, npj Quantum Inf. **11**, 5 (2025).

[28] W. Wernsdorfer, From micro- to nano-SQUIDs: Applications to nanomagnetism, Supercond. Sci. Technol. **22**, 064013 (2009).

[29] J. G. Kroll, F. Borsoi, K. L. van der Enden, W. Uilhoorn, D. de Jong, M. Quintero-Pérez, D. J. van Woerkom, A. Bruno, S. R. Plissard, D. Car, E. P. A. M. Bakkers, M. C. Cassidy, and L. P. Kouwenhoven, Magnetic-field-resilient superconducting coplanar-waveguide resonators for hybrid circuit quantum electrodynamics experiments, Phys. Rev. Appl. **11**, 064053 (2019).

[30] N. Samkharadze, A. Bruno, P. Scarlino, G. Zheng, D. P. DiVincenzo, L. DiCarlo, and L. M. K. Vandersypen, High-kinetic-inductance superconducting nanowire resonators for circuit QED in a magnetic field, Phys. Rev. Appl. **5**, 044004 (2016).

[31] A. Bahr, M. Boselli, B. Huard, and A. Bienfait, Improving magnetic-field resilience of NbTiN planar resonators using a hard-mask fabrication technique, Appl. Phys. Lett. **124**, 114004 (2024).

[32] D. Niepce, J. Burnett, and J. Bylander, High kinetic inductance NbN nanowire superinductors, Phys. Rev. Appl. **11**, 044014 (2019).

[33] S. Frasca, I. N. Arabadzhiev, S. Y. B. de Puechredon, F. Oppliger, V. Jouanny, R. Musio, M. Scigliuzzo, F. Minganti, P. Scarlino, and E. Charbon, NbN films with high kinetic inductance for high-quality compact superconducting resonators, Phys. Rev. Appl. **20**, 044021 (2023).

[34] T. Charpentier, D. Perconte, S. Léger, K. R. Amin, F. Blondelle, F. Gay, O. Buisson, L. Ioffe, A. Khvalyuk, I. Poboiko, M. Feigel'man, N. Roch, and B. Sacépé, First-order quantum breakdown of superconductivity in an amorphous superconductor, Nat. Phys. **21**, 104 (2025).

[35] K. Borisov, D. Rieger, P. Winkel, F. Henriques, F. Valenti, A. Ionita, M. Wessbecher, M. Spiecker, D. Gusenkova, I. M. Pop, and W. Wernsdorfer, Superconducting granular aluminum resonators resilient to magnetic fields up to 1 Tesla, Appl. Phys. Lett. **117**, 120502 (2020).

[36] L. Grünhaupt, N. Maleeva, S. T. Skacel, M. Calvo, F. Levy-Bertrand, A. V. Ustinov, H. Rotzinger, A. Monfardini, G. Catelani, and I. M. Pop, Loss mechanisms and quasiparticle dynamics in superconducting microwave resonators made of thin-film granular aluminum, Phys. Rev. Lett. **121**, 117001 (2018).

[37] I. Siddiqi, Engineering high-coherence superconducting qubits, Nat. Rev. Mater. **6**, 875 (2021).

[38] G. Deutscher, H. Fenichel, M. Gershenson, E. Grünbaum, and Z. Ovadyahu, Transition to zero dimensionality in granular

aluminum superconducting films, J. Low Temp. Phys. **10**, 231 (1973).

[39] N. Maleeva, L. Grünhaupt, T. Klein, F. Levy-Bertrand, O. Dupre, M. Calvo, F. Valenti, P. Winkel, F. Friedrich, W. Wernsdorfer, A. V. Ustinov, H. Rotzinger, A. Monfardini, M. V. Fistul, and I. M. Pop, Circuit quantum electrodynamics of granular aluminum resonators, Nat. Commun. **9**, 3889 (2018).

[40] J. Luomahaara, V. Vesterinen, L. Grönberg, and J. Hassel, Kinetic inductance magnetometer, Nat. Commun. **5**, 4872 (2014).

[41] A. T. Asfaw, E. I. Kleinbaum, T. M. Hazard, A. Gyenis, A. A. Houck, and S. A. Lyon, SKIFFS: Superconducting kinetic inductance field-frequency sensors for sensitive magnetometry in moderate background magnetic fields, Appl. Phys. Lett. **113**, 172601 (2018).

[42] S. Sypkens, F. Faramarzi, M. Colangelo, A. Sinclair, R. Stephenson, and J. Glasby, Development of an array of kinetic inductance magnetometers (KIMs), IEEE Trans. Appl. Supercond. **31**, 1 (2021).

[43] F. K. Larsen, E. J. L. McInnes, H. E. Mkami, J. Overgaard, S. Piligkos, G. Rajaraman, E. Rentschler, A. A. Smith, G. M. Smith, V. Boote, M. Jennings, G. A. Timco, and R. E. P. Winpenny, Synthesis and characterization of heterometallic {Cr_7M} wheels, Angew. Chem. **115**, 105 (2003).

[44] A. Ardavan, O. Rival, J. J. L. Morton, S. J. Blundell, A. M. Tyryshkin, G. A. Timco, and R. E. P. Winpenny, Will spin-relaxation times in molecular magnets permit quantum information processing? Phys. Rev. Lett. **98**, 057201 (2007).

[45] G. A. Timco, S. Carretta, F. Troiani, F. Tuna, R. J. Pritchard, C. A. Muryn, E. J. L. McInnes, A. Ghirri, A. Candini, P. Santini, G. Amoretti, M. Affronte, and R. E. P. Winpenny, Engineering the coupling between molecular spin qubits by coordination chemistry, Nat. Nanotechnol. **4**, 173 (2009).

[46] S. Günzler, J. Beck, D. Rieger, N. Gosling, N. Zapata, M. Field, S. Geisert, A. Bacher, J. K. Hohmann, M. Spiecker, W. Wernsdorfer, and I. M. Pop, Spin environment of a superconducting qubit in high magnetic fields, arXiv:2501.03661.

[47] D. Rieger, S. Günzler, M. Spiecker, P. Paluch, P. Winkel, L. Hahn, J. K. Hohmann, A. Bacher, W. Wernsdorfer, and I. M. Pop, Granular aluminium nanojunction fluxonium qubit, Nat. Mater. **22**, 194 (2023).

[48] B. Ho Eom, P. K. Day, H. G. LeDuc, and J. Zmuidzinas, A wideband, low-noise superconducting amplifier with high dynamic range, Nat. Phys. **8**, 623 (2012).

[49] D. Abraham, G. Deutscher, R. Rosenbaum, and S. Wolf, Characteristics of granular Al-Al_2O_3 SQUIDs, J. Low Temp. Phys. **32**, 853 (1978).

[50] M. Gershenson and W. L. McLean, Magnetic susceptibility of superconducting granular aluminum, J. Low Temp. Phys. **47**, 123 (1982).

[51] I. Chiorescu, W. Wernsdorfer, A. Müller, H. Bögge, and B. Barbara, Butterfly hysteresis loop and dissipative spin reversal in the $S = 1/2$, V_{15} molecular complex, Phys. Rev. Lett. **84**, 3454 (2000).

[52] W. Wernsdorfer, D. Mailly, G. A. Timco, and R. E. P. Winpenny, Resonant photon absorption and hole burning in Cr_7Ni antiferromagnetic rings, Phys. Rev. B **72**, 060409(R) (2005).

[53] D. H. Douglass, Magnetic field dependence of the superconducting energy gap, Phys. Rev. Lett. **6**, 346 (1961).

[54] J. J. Burnett, A. Bengtsson, M. Scigliuzzo, D. Niepce, M. Kudra, P. Delsing, and J. Bylander, Decoherence benchmarking of superconducting qubits, npj Quantum Inf. **5**, 54 (2019).

[55] A. Somoroff, Q. Ficheux, R. A. Mencia, H. Xiong, R. Kuzmin, and V. E. Manucharyan, Millisecond coherence in a superconducting qubit, Phys. Rev. Lett. **130**, 267001 (2023).

[56] D. Rieger, S. Günzler, M. Spiecker, A. Nambisan, W. Wernsdorfer, and I. M. Pop, Fano interference in microwave resonator measurements, Phys. Rev. Appl. **20**, 014059 (2023).

[57] V. Gupta, P. Winkel, N. Thakur, P. van Vlaanderen, Y. Wang, S. Ganjam, L. Frunzio, and R. J. Schoelkopf, Low-loss lumped-element inductors made from granular aluminum, Phys. Rev. Appl. **23**, 054067 (2025).